Framework for rapid design and optimisation of immersive battery cooling system

Ali Almshahy[1,2*], Z. Khatir[1,@], K. J. Kubiak[1,$], and M. Al Qubeissi[3]

[1]School of Mechanical Engineering, Faculty of Engineering and Physical Sciences,
University of Leeds, LS2 9JT, Leeds, UK.
[*]fsvl1319@leeds.ac.uk, [@]z.khatir@leeds.ac.uk, [$]k.kubiak@leeds.ac.uk
[2] Inspection and Asset Integrity Department, Zubair Field Operating Division,
Basra Oil Company (BOC), Ministry of Oil, Basra 240, Iraq.
[2]alebadi899@gmail.com
[3] Department of Mechanical Engineering, College of Engineering & Technology,
University of Doha for Science and Technology, P. O. Box 24449, Doha, Qatar.
[3]mansour.alqubeissi@udst.edu.qa

Abstract

Effective battery thermal management system (BTMS) is critical for lithium-ion battery (LIB) safety and performance in electric vehicles. This study presents a CFD-driven optimisation framework for an immersion cooling BTMS using sustainable palm biodiesel as coolant. The Multi-scale Multi-Domain (NTGK) framework is conducted to effectively capture the complex interactions among various physicochemical processes. The Electrochemical-thermal Model (ECM) is applied using the Newman, Tiedeman, Gu, and Kim (NTGK) model. A conjugate heat transfer model for a 3S2P pouch cell module (20 Ah $LiFePO_4$) is developed and validated against experimental data (<2% error). The CFD model of a battery module is developed to train an ultra-fast metamodel for battery geometry optimisation. Two key parameters are optimised, namely: battery gap spacing (3-10 mm) and inlet/outlet width (5-15 mm), via Optimal Latin Hypercube Sampling, Support Vector Regression, and GDE3 algorithm. Palm biodiesel is used as a dielectric coolant in the proposed system to preserve LIB temperature within 20-40 ℃, preventing thermal runaway and ensuring a lightweight BTMS design. Compared to a conventional 3M-Novec, the palm biodiesel achieved system lightweight by 43%. The findings can establish biofuel immersion cooling as an eco-friendly BTMS solution, achieving Pareto-optimal figures: T_{max} < 29.9°C, ΔT < 5°C, and ΔP < 145.275 Pa (at 5C and 0.05 m/s).

Key words: *Battery thermal management, Biodiesel coolant, Hybrid electric vehicles, Immersion cooling, Optimisation, Surrogate modelling.*

Article Highlights

- First biodiesel-based BTMS immersion cooling is developed.
- The novel experimentally validated computational model offers enhanced cooling over conventional coolants.
- Machine learning via RBF-assisted SVR enables rigorous multi-objective optimisation.
- Pareto curves show trade-offs between maximum temperature, temperature difference, and pressure drop.

1. Introduction

Lithium-Ion Batteries (LIBs) serve as critical enablers for decarbonisation across the automotive, renewable energy, and consumer electronics sectors. Their rapid development is driven by global commitments to net-zero emissions, exemplified by the UK's 2050 target [1]. However, the key challenges persist in operational safety, temperature uniformity, lifespan, and recyclability [2]. Effective Battery Thermal Management Systems (BTMS) are paramount to address these issues, as uncontrolled temperature rise (>40°C) that accelerates degradation while thermal runaway risks catastrophic failure [3].

A considerable amount of heat is generated within a LIB battery during the high discharge process, resulting from exothermic chemical reactions [4]. To ensure optimal performance, it is crucial to effectively dissipate the heat generated, directing it from the LIB surface to the metallic tabs. Consequently, a range of advanced cooling strategies for the BTMS have been explored: air cooling [5], indirect liquid cooling [6], and phase change materials [7]. Implementing these solutions will significantly enhance the system's efficiency and reliability. Despite their

advantages, BTMS-based air, indirect liquid and PCM cooling techniques experience inherent limitations: Air cooling provides inadequate heat dissipation for high-density packs [8], Phase-Change Materials (PCMs) suffer from low thermal conductivity under high loads [9]. While indirect liquid cooling exhibits superior thermal performance, the system design is relatively bulky and complex [10]. Furthermore, it introduces parasitic weight and interfacial thermal resistance between battery surface and cold plate which leads to degraded heat transfer rate [11].

An innovative and powerful alternative cooling strategy to BTMS is direct liquid cooling, known as immersion cooling. By eliminating thermal interfaces, this approach achieves superior temperature uniformity (±2°C) and heat transfer coefficients (HTCs >500 W/m²·K), significantly outperforming existing methods [12], [13]. Recent studies validate its efficacy: Kim et al. demonstrated mineral oil's 40% higher heat removal versus air cooling [14], Haosheng et al. illustrated that transformer oil and PAO-4 show superior cooling performance even at extensive conditions [15], while Al Qubeissi et al. showed fuel-based immersion reduced peak temperatures by 5.6% at 2C discharge [16, 17]. BTMS-based immersion cooling is an effective approach to preserving the operating temperature within the safety limit.

A variety of optimisation approaches have been conducted to improve the BTMS-based immersion cooling. Zhu et al. [18] conducted various surrogate models (i.e., Kriging, ANN, and radial basis function) and multi objective optimisation using NSGA-‖ to enhance the thermal performance. The results revealed that the maximum temperature and temperature difference were reduced by 5.41% and 7.76, respectively, compared to the benchmark results. While the pressure drops incremented by 22.98%. Adeniran et al. [19] studied different configuration of BTMS-based immersion cooling. They optimised U-type configuration using Kriging surrogate model and Multi objective Genetic Algorithm (MOGA). The results confirmed that the temperature difference increased by 39 %, though pressure drop and module volume reduced by 28% and 6%, respectively. Another optimisation study conducted by [20], using various metamodels (i.e., Gaussian process, radial basis function, and response surface model) and muti objective optimisation (NSGA-‖) to find the optimal solutions. The results indicated that the maximum temperature and temperature difference remined within the operating conditions.

As one can see from the previous studies, significant progress has been performed in the BTMS-based immersion cooling. However, some research gaps remain unexplored, to address these: (1) Conventional dielectric coolants (e.g., hydrofluoroethers, silicone oils) present sustainability trade-offs through high Global Warming Potential (GWP) and resource-intensive synthesis [17]. Hence, the current study focuses more on sustainable and environmentally friendly coolants. Aiming to synergize these sustainable coolants with computational optimisation to achieve the high thermal performance and environmental targets. Biodiesel, particularly palm oil, variants offer an eco-friendly alternative with competitive thermophysical properties (k ≈ 0.16-0.18 W/m·K, cp >1900 J/kg·K) and 43% weight reduction versus fluorinated fluids [21]. Critically, it maintains cells within the 20–40°C operational window while enhancing biodegradability [22]. (2) System-level optimisation of biodiesel-based immersion cooling remains underexplored, especially regarding geometric and flow parameter trade-offs. (3) The existing research primarily concentrates on the aforementioned surrogate models and multi-objective optimisations, with insufficient consideration of the Support Vector Regression (SVR) surrogate model along with the Generalised Differential Evolutionary Algorithm (GDE3).

Multi-Objective Optimisation (MOO) is conducted using Generalised Differential Evolutionary Algorithm (GDE3) to optimise and analyse the metamodels. GDE3 is a robust algorithm that can handle the optimisation framework, including multi-model and non-linear functions [23]. Its convergence characteristics are faster than traditional algorithms as a result of using advanced strategies that regulate the problem landscape. GDE3 outperforms many different (MOO) algorithms in terms of accuracy and convergence speed for optimisation frameworks [24, 25]. In addition, it can handle complex problems due to its adaptive strategies and population diversity. Therefore, GDE3 is a powerful optimisation tool used to handle the global optimisation with any number of constraints and goals [23].

Following author's pervious study [21], this study bridges this gap through a CFD-driven optimisation framework for a 3S2P LIB module (20 Ah pouch cells) using palm biodiesel coolant. Additionally, we parameterise two key variables: battery gap spacing (thermal uniformity), and inlet/outlet width (pressure drop). Support Vector Regression (SVR) with a Radial Basis (RBF) surrogate model trained on DOE simulations enables efficient multi-objective optimisation via a Generalized Differential Evolutionary Algorithm (GDE3), generating Pareto-optimal solutions that can balance: maximum temperature suppression (<40°C), cell-to-cell temperature differential (ΔT <5°C), and pumping power minimisation (ΔP reduction).

Our work advances BTMS design by demonstrating how sustainable coolants synergise with computational optimisation to achieve lightweight, high-performance thermal management, helping to address both operational safety and environmental goals. In what follows: the mathematical model and the parameters' setup are demonstrated

in section 2, the design optimisation analysis is described in section 3, the results of BTMS and data analysis are presented in section 4, and the findings of data analysis are summarised in section 5.

2. Research Methodology

2.1 LIB system configuration

LIBs are rechargeable batteries used in EVs, storage systems, and electronic products. They exhibit several merits among other battery types, for instance, lead-acid and nickel-cadmium batteries [22]. LIBs are preferred choices as a result of high-power capacity, high energy density, lightweight construction, long life cycle, and less self-discharge [26]. Three fundamental formats characterize the manufacturing landscape of LIBs [27]: (i) cylindrical cell, (ii) prismatic cell, and (iii) pouch cell. Table 1 provides a contrast of three types of cells in terms of electrical and physical parameters. Pouch cell is chosen for the current battery pack study over other types because of low internal resistance and high energy density. Furthermore, it was determined that the Lithium Iron Phosphate (LFP) pouch cell is the most suitable based on chemistry specification compared to other cells, as shown in Table 2.

Table 1. Physical and electrical parameters of battery cell [28].

Cell type	Thermal management	Packing efficiency	Internal resistance
Pouch	Easy	High	Low
Cylindrical	Moderate	Low	High
Prismatic	Difficult	Medium	Medium

Tabel 2. Cell specification riles on chemistry [29, 30].

LIB type	Specific power	Specific energy	Safety	Life span	Cost
LFP	High	Low	High	High	Low
LCO	High	High	Low	Low	Low
NMC	Moderate	High	Moderate	Moderate	Low
NCA	Moderate	High	Low	Moderate	Moderate

Note: LFP: lithium iron phosphate, LCO: lithium cobalt oxide, NMC: lithium nickel manganese, NCA: lithium nickel cobalt aluminium oxide.

2.2 Multiphysics modelling framework

The numerical simulation is considered significant for analysing the BTMS and comparing battery thermal behaviour under several operating conditions. The present study primarily focuses on pouch cell 20 Ah with 3S2P module configurations to gain crucial results in a reasonable time and save computational effort. Ansys Fluent (2024/R2) was employed to carry out numerical simulations, and an integrated Electrochemical-thermal Model (ECM) and battery module with the proposed system were investigated.

Modelling of Li-ion batteries is a challenging and complex problem due to inherent Multi-Scale Multi-Domain (MSMD) character along with different length scales involved [31]. Thermal analysis emphasises on temperature spreading across the battery's length scale, whereas Li-ion transfer within the active material takes place at the atomic length scale. Conducting numerical study computationally is expensive due to involving interplay of multi-process, i.e., physiochemical-thermal-electrical. In this study, the MSMD approach is leveraged in the design for several physical systems in different solution domains. For represent and simulate the ECM, the Newman, Tiedemann, Gu, and Kim (NTGK) model is used, which is semi-empirical electrochemical model proposed by [17], [32]. NTGK is an effective model for Li-ion batteries and has several merits, for example, highly efficient of numerical results, match experimental data, less computational cost. Particularly, it has extensively used for Pouch/Prismatic cells [33]. Therefore, new numerical approach was developed employing the MSMD approach and using NTGK model.

In the present study, a 3D transient modelling study is conducted to simulate Lithium-ion batteries with their enclosure utilising a CFD software. The system is designed using Design modeller in ANSYS V2024/R2 to represent a 20Ah (LFP) commercial Li-ion battery pouch cell. To reduce computational effort while obtaining significant results in

considerable time and accomplish a 3S2P battery configuration, the battery module consists of six cells as following published works [20, 34]. Battery module is arranged as three cells in series and two in parallel (3s2p), as shown in Figure 1. Configuration of four cells in series yield incrementing the module voltage, while two cells in parallel connection leads to increase in module capacity, which significantly contributed to slow down the discharge time. The cells are attached to tabs and busbar to form one module. The model benchmark designs the battery space is set to 5 mm giving the HTC and fluid flow efficiency to cool down battery cells and fulfil the homogeneity. The Li-ion cell thermophysical specifications are listed in Table 3.

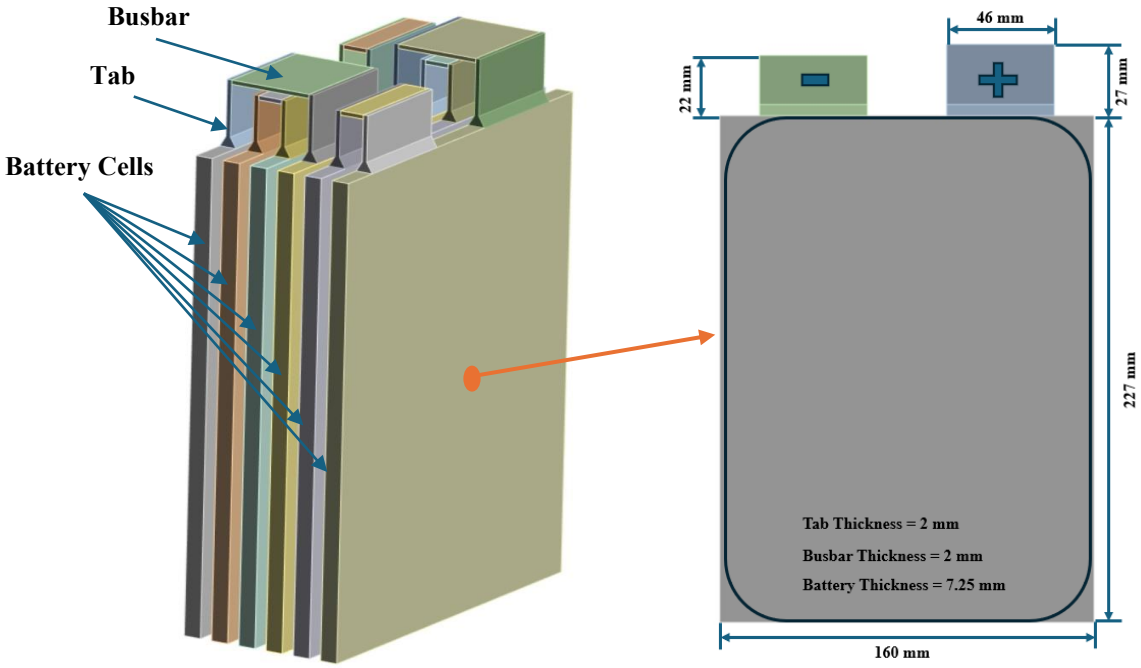

Fig. 1 Schematic of the battery module (in 3S2P configuration)

Tabel 3. LIB pouch cell specifications used in this study [31].

Battery cell specification		Positive and Negative tab	
Nominal Cell Capacity (Ah)	20	Positive Tab & Busbar	
Max Voltage (V)	3.6	Density (kg/m^3)	2719
Min Voltage (V)	2	Thermal Conductivity (W/m.K)	202
Nominal Voltage (V)	3.3	Specific Heat (J/kg.K)	871
Height (mm)	227		
Width (mm)	160	Negative Tab	
Thickness (mm)	7.25	Density (kg/m^3)	8978
Density (kg/m^3)	1868	Thermal Conductivity (W/m.K)	387.6
Specific Heat (J/kg.K)	1067	Specific Heat (J/kg.K)	381
Thermal Conductivity (W/m.K)	Anisotropic (K_{xx},K_{yy}=28, K_{zz}=0.8)		
Cathode material	$LiFePO_4$		
Anode material	Graphite		

An enclosure was designed to partially immerse the LIBs pouch cells. A rectangular inlet and outlet with flow guides

were employed to direct coolants around the battery cells for better performance. The outer wall of the fluid domain is strategically designed as an adiabatic wall for the numerical analysis of the 3S2P battery module. Also, the enclosure is designed as a dielectric fluid domain (DF) which enhances the capability to quickly simulate solutions for CFD and accelerates the modelling process and ensures more effective and timely results, as referenced in [31, 35]. This approach would ensure coolants coming in direct contact with surface of the cells, thus decreasing the thermal resistance and increasing the thermal homogeneity. Figure 2 shows an example of enclosure configuration. Therefore, the main objective is to maximise even temperature distribution and minimise any hot spots, hence it would improve power capacity and thermal performance of the module.

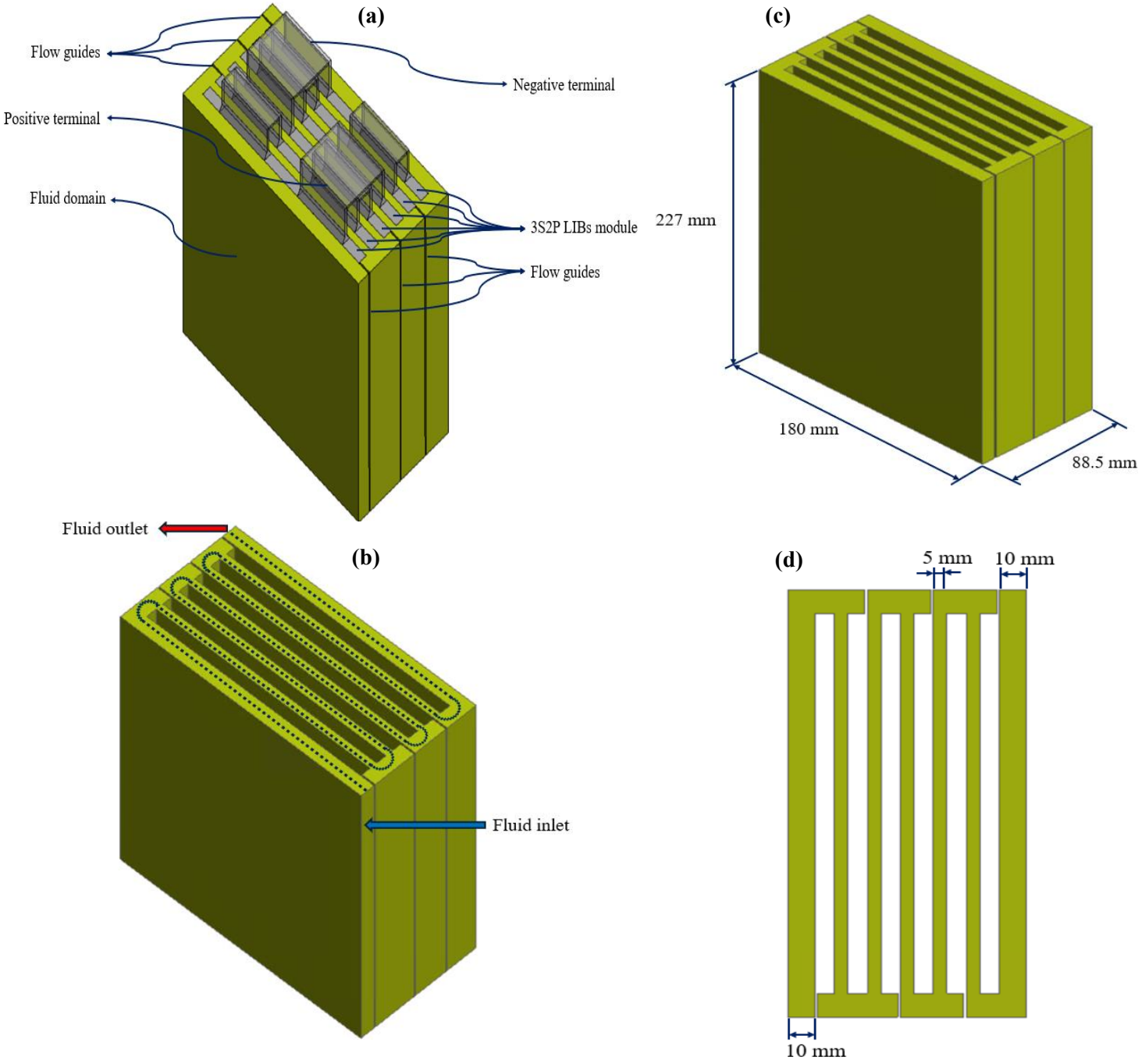

Fig. 2 Example of the battery module enclosure (h_b=5mm, W_c=10mm), (a) battery module along with fluid domain, (b) represents the flow orientation, (c) and (d) enclosure dimensions.

2.3 CFD model

LIB temperature distribution is computed depend on the energy conservation equation as expressed in equation 1. Equation 2 & 3 show the current flux at the positive and negative electrode, respectively. Electrochemical reaction heat is computed as written in equation 4. In addition, the current density $J_{\dot{E}ch}$ and depth of discharge (DOD) of battery cell are calculated from equations 5 & 6, respectively.

$$\frac{\partial \rho c_p T}{\partial t} - \nabla \cdot (K \nabla T) = \sigma_+ |\nabla \varphi_+|^2 + \sigma_- |\nabla \varphi_-|^2 + q_{\dot{E}Ch}, \quad (1)$$

$$\nabla \cdot (\sigma_+ \nabla \varphi_+) = -J_{\dot{E}ch}, \quad (2)$$

$$\nabla \cdot (\sigma_- \nabla \varphi_-) = J_{\dot{E}ch}, \quad (3)$$

$$q_{\dot{E}Ch} = J_{\dot{E}ch} \left[(U - V) - T \frac{dU}{dT} \right], \quad (4)$$

$$J_{\dot{E}ch} = \frac{Q_{\text{nominal}}}{Q_{ref}} Y[U - V], \quad (5)$$

$$DOD = \frac{V_{ol_b}}{3600 Q_{nominal}} \int_0^t j \, dt. \quad (6)$$

Where ρ, T, K, C_p and are density, temperature, thermal conductivity, and specific heat capacity of the battery, correspondingly. $q_{\dot{E}ch}$ referred to the electrochemical reaction heat. $\sigma_+ and\ \sigma_-$ are electrical conductivity of positive and negative electrodes, respectively. $\varphi_- and\ \varphi_-$ are phase potential of electrodes. $J_{\dot{E}ch}$ is the volumetric current transfer due to electrochemical reaction.

Q_{nominal} is the nominal cell capacity and Q_{ref} is the cell capacity used to obtain the value of Y and U in the experimental work, which represents the depth of discharge functions. The battery fitting parameters U and Y are obtained from experimental published data by Patil et al. [31]. They investigated an experimental study to calculate the heat generation rate of battery cell (20 Ah, $LiFePO_4$) at 3C-dicharge rate and ambient temperature 25 ℃. The correlation fitting parameters with DOD functions are therefore expressed as:

$$U = 3.462647 - 3.87924\,(\text{DOD})^1 + 22.9369(\text{DOD})^2 - 60.0521(\text{DOD})^3 + 70.26211(\text{DOD})^4 - 30.2737(\text{DOD})^5, \quad (7)$$

$$Y = 131.2422 + 28.57686\,(\text{DOD})^1 - 266.689(\text{DOD})^2 + 955.2629(\text{DOD})^3 - 1347.92(\text{DOD})^4 + 573.8234(\text{DOD})^5. \quad (8)$$

The thermophysical properties of dielectric immersion cooling, including specific heat, thermal conductivity, and viscosity, were assumed constant. In addition, the dielectric immersion flow was assumed incompressible that ensuring no depletions or accumulations of mass flow within the control volume. The detailed of system boundary conditions are described in the Table 4. For immersion cooling study, fluid flow models are incorporated alongside the thermal and electrochemical model. Fluids governing equations for momentum, continuity, and energy can be expressed in equations 9, 10, and 11, respectively [36].

$$\frac{\partial \rho_c}{\partial t} \mathcal{V}_c + \nabla(\mathcal{V}_c . \rho_c)\mathcal{V}_c = -\nabla p + (\mu_c \nabla \mathcal{V}_c), \quad (9)$$

$$\nabla . \mathcal{V}_c = 0, \quad (10)$$

$$\rho_b C_{p,b} \frac{\partial T_c}{\partial t} + \nabla . (\rho_b C_{p,b} \mathcal{V}_c T_c) = \nabla . (K_c \nabla T_c). \quad (11)$$

Where μ_c, p, K_c, T_c, C_p, $\mathcal{V}_c$, ρ_c are dynamic viscosity, static pressure, thermal conductivity, temperature, specific heat capacity, velocity, and density, respectively.

Table 4. Dielectric fluid boundary conditions.

Specifications	Values
Coolant	Dielectric fluid (biodiesel)
Inlet coolant temperature (ºC)	25
Initial Temperature (ºC)	25
Inlet coolant velocity (m/s)	0.01, 0.05, & 0.09

Discharge-rate	2C, 3C, & 5C
Inlet coolant velocity (m/s) for optimisation	0.05
Discharge-rate for optimisation	5C
Flow model	Laminar flow
Inlet condition	Velocity
Outlet condition	Atmospheric pressure
Wall boundary condition	No-slip wall

In this study, the thermophysical properties of biodiesel-palm are regarded as constant. The fluid is assumed to be incompressible that refers to the density remaining constant throughout the flow. The flow model is laminar based on the Reynolds numbers (300 < Re <1000). The inlet and outlet for dielectric fluid are regarded as inlet velocity and atmospheric pressure, respectively. LIBs heat generated during the discharging process are regarded as the heat source. Battery module free convection with heat transfer coefficients equal to 10 ($W/m^2.K$). Numerical simulations are conducted via ANSYS-fluent V-2024R2 with finite volume method (FVM). The convergence criteria for the continuity, momentum, and energy equations' residuals are set to 10^{-3}, 10^{-3}, and 10^{-6}, respectively, to ensure the accuracy of the numerical results. A transient thermal model was simulated at 1s time step size and 20 number of iterations until the battery module fully discharged. The outer wall of the fluid domain is treated as an adiabatic wall for the numerical study of the 3S2P battery module. The enclosure is viewed as a dielectric fluid domain, which enhances the capability to quickly simulate solutions for computational fluid dynamics (CFD), which accelerates the modelling process and ensures more effective and timely results. Furthermore, the set-ups and pre-processing of the CFD simulations are provided in the Table 5.

Table 5. CFD simulation set-ups.

Physics	1. Time: Transient	Initialization	Standard Initialization
	2. Type: Pressure-Based	Transient Set-up	1. Type: Fixed
	3. Velocity Formation: Absolute		2. Method: User-specified
Battery Module	1. Solution Method: MSMD		3. Time Step Size (s): 1
	2. E-Chemistry: NTGK Model		4. Max Iterations/Time Step: 20
	3. Solution Options: Specified C-Rate		5. Reporting Interval: 1
	4. Echem Stop Criterion: Voltage	Solution Methods	1. Scheme: SIMPLE
Solutions Equations	1. Flow		2. Gradient: Least Squares cell Based
	2. Energy		3. Pressure: Second Order
	3. Potential Ph+		4. Momentum: Second Order Upwind
	4. Potential Ph-		5. Energy: Second Order Upwind
Residual Monitors	1. Continuity Equation (10^{-3})		6. User Scalar 0: First Order Upwind
	2. Momentum Equation (10^{-3})		7. User Scalar 1: First Order Upwind
	3. Energy Equation (10^{-6})		8. Transient Formulation: Second Order Implicit

The thermal-fluid model integrates fundamental physical domains: Electrochemical-thermal Model (ECM) heat generation within cells, convective heat transfer at coolant-cell interfaces, and hydrodynamics behaviour within the enclosure. Convective heat transfer in the fluid boundary region can be expressed in equation 12.

$$\dot{Q}_{conv} = \text{h A } (T_s - T_\infty) \quad (12)$$

where h & A are heat transfer cofficients and LIB surface area, resepctively. T_s & T_∞ are the surface temperature and fluid free stream temperature, correspondingly.

Boundary layer development governs convective efficiency. The Reynolds number characterizes flow regime and scaling:

$$\mathrm{Re} = \frac{\rho v D_h}{\mu} \tag{13}$$

Analysing heat transfer characteristics of immersion cooling system are assessed relied on battery cell maximum temperature, temperature variation, and pressure drop. Temperature variation, pressure drop, and power consumption can be calculated using equations 14, 15, and 16 [34, 37, 38], respectively.

$$\Delta T(t) = \max\{T_i(t)\} - \min\{T_i(t)\}, i \in \{1,2,3,4,5,6\}, \tag{14}$$

$$\Delta P = P_{in} - P_{out}, \tag{15}$$

$$\mathrm{Power} = \Delta P \times A \times v. \tag{16}$$

Thermal conductivity is essential to conduct heat. LIBs are affected by chemical reaction and their layered structures. Hence, thermal conductivity presents a highly orthotropic behaviour in real scenarios for batteries [39, 40]. The anisotropic thermal conductivity of pouch battery cell is represented by equation 17 [40].

$$K_b = \begin{bmatrix} Kxx & 0 & 0 \\ 0 & Kyy & 0 \\ 0 & 0 & Kzz \end{bmatrix} = \begin{bmatrix} 28 & 0 & 0 \\ 0 & 28 & 0 \\ 0 & 0 & 0.8 \end{bmatrix} \tag{17}$$

2.4 Mesh independence check

A CFD simulation necessitates a high-fidelity mesh and convergence criteria to attain accuracy and reliable results. Figure 3 depicts 3D-tetrahedral grids that are applied to the computational module. A boundary layer with a 1.2 inflation rate is introduced between fluid domain and solid wall to anticipate an increase in velocity in this layer. Mesh validation was conducted at constant inlet velocity of 0.09 m/s and 3C discharge rate with increasing number of elements to establish sufficient model size. Figure 4 shows comparisons among five different grids, with total number of elements: 498481, 661990, 1290410, 3557688, and 4931316, respectively. Results show that a grid with 3557688 cells ensures convergence balance between simulation accuracy and time by comparing maximum battery temperature and pressure drop. In addition, orthogonal mesh quality is accounted to ensure the mesh quality. The maximum and minimum value were 0.99 and 0.154, respectively, which are acceptable values for the numerical simulations [41]. Therefore, with this grid size conducted simulations for all cases.

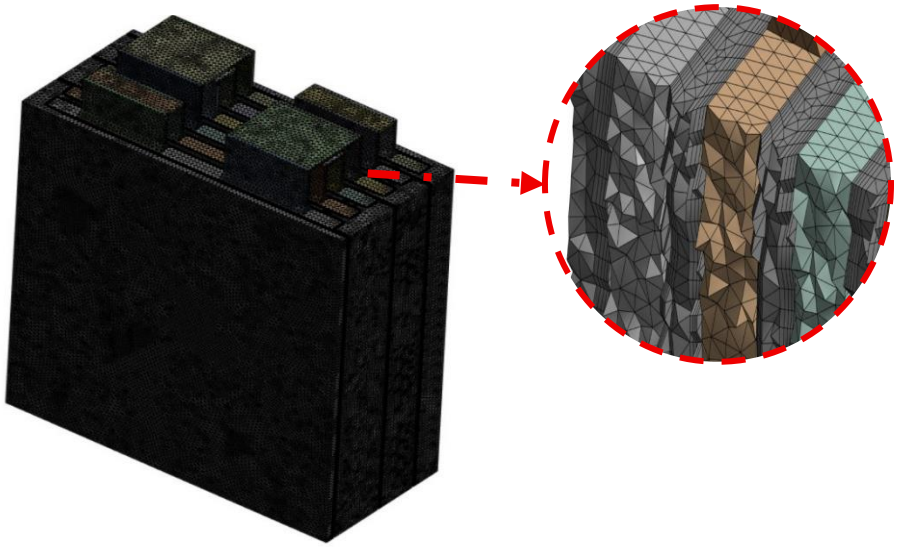

Fig. 3 Example of mesh configuration of 3S2P battery module

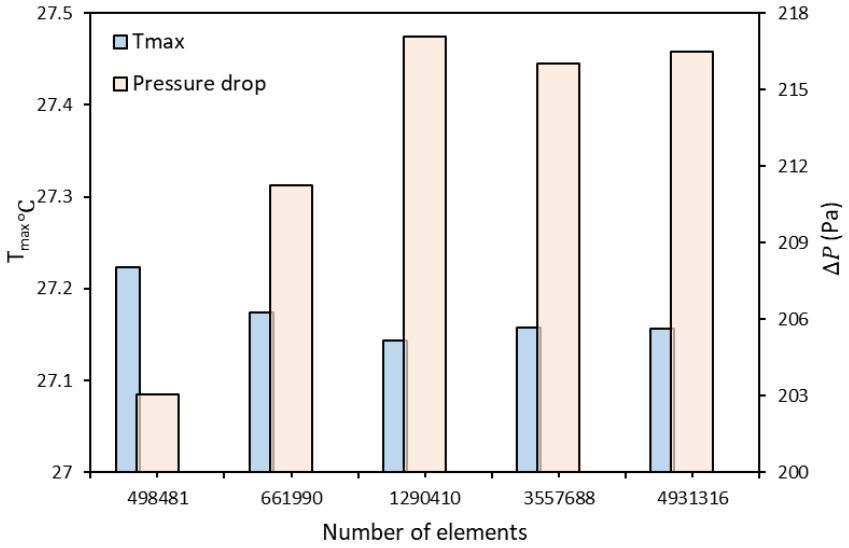

Fig. 4 Mesh independence study

2.5 Biodiesel Coolants

Biodiesels are considered an alternative fuel that are produced from natural resources, for instance plants, oils, and animals' fats [42]. They are less harmful as compared with fossil fuels and environmentally friendly that make them an interesting alternative in HEV [42]. In the previous work [21], authors investigated four types of biodiesels for BTMS, namely Palm, Jatropha, Mahua, and Karanja, then they were compared with traditional air cooling and immersive using 3M-Novec 7100 as fluid. The Novec fluids are a series of hydrofluoroether products developed by 3M, known for their wide range of thermal properties [1]. Recently, hydrofluoroethers have gained significant attention in electronic immersion cooling and have been applied to BTMS [43, 44, 45, 46]. Researchers have utilized 3M-Novec 7100 in immersion cooling applications for BTMS due to its non-flammable nature, excellent thermal controllability, non-corrosive, low global warming potential (GWP), and zero ozone depletion potential (ODP) [47], which significantly mitigate thermal runaway and enhance system safety [48, 49]. Therefore, 3M-Novec 7100 was chosen for comparison with biodiesel in this study.

Among the biodiesel tested, palm biodiesel demonstrated the best cooling performance, outperforming both the biodiesel alternative and conventional cooling systems. It maintained the LIB within the temperature range 20 – 40 °C, and effectively preventing thermal-runaway. As a result, this led to a 43% lighter BTMS design compared to the conventional 3M-Novec [21]. Therefore, the palm-based biodiesel is used as coolant in this study, thermodynamic properties of coolant are shown in the Table 6.

Table 6. Comparison of thermodynamic properties of palm biodiesel coolant and traditional coolants [21].

Coolants properties	Cooling Fluids		
	Palm	3M-7100	Air
Density (kg/m3)	865	1510	1.225
Viscosity (Kg/m.s)	0.0039	0.0006	0.0000179
Thermal Conductivity (W/m.K)	0.172	0.069	0.025
Specific Heat (J/kg.K)	1687.248	1183	1006.43

To comprehensively assess the cost and environmental impacts aspects of biodiesel and 3M-7100, the key findings are summarized in Table 7. The table demonstrates that biodiesel has lower initial cost and simpler structure than 3M-Novec 7100. In addition, it is regarded as environmentally friendly and offered enhanced safety. Thus, biodiesel is considered as promising solution and more suitable for BTMS, which can significantly improve temperature field and heat dissipation of battery module. Although higher kinematic viscosity of biodiesel may lead to increase system power consumption, its lower cost and maintenance due to simple structure might compensate for this shortage.

Table 7. Comparison between biodiesel and 3M-Novec 7100 in terms of environmental and cost aspects [17].

Factor	3M-Novec 7100	Biodiesel fuel
Cost per litter	$50 - $100 USA	$4 - $7 USA
Toxicity	Low toxicity and environmental safety	environmentally friendly
System requirements	Complex structure and system design (increase maintenance cost)	Simple structure (fatty acid methyl esters)
Weight Consideration	Relatively high (increase overall weight of system)	Relatively lighter than conventional coolants
Biodegradability	Low (low global warming potential)	More biodegradable (minimizes environmental impact in case of spills)

3. Design Optimisation of Immersion Cooling

The main aim of optimisation methodology is to select the design variables which influence BTMS performance. Besides, they are minimising power consumption with maintaining the battery operation in a proper range for maximum temperature and temperate uniformity. Thus, to fulfil this a surrogate model is employed.

3.1 Surrogate Modelling

Design optimisations use a surrogate model as a significant tool to produce approximations for computationally expensive and complex models by using a limited number of parameters from the original model. In the present study, a mathematical model was created by using surrogate approach to select design variables and target objectives.

Optimal Latin Hypercube Sampling (OLHS) was employed to obtain a surrogate model. It is widely utilised among other models due to its ability to fill the entire design space [42, 50]. To achieve the filling property, optimal criteria namely Enhanced Stochastic Evolutionary Algorithm (ESE) is considered in the present work, which is developed by Jin et al., [51]. ESE algorithm is composed of two loops (i.e., the inner and outer loop). The inner loop creates a new design through element exchange and evaluates the design based on a specified acceptance criterion. While the outer loop regulates the optimisation process by controlling the threshold $\mathbf{T_h}$ in the acceptance criterion.

Several parameters influence BTMS performance and selecting all of them leads to an increase in the computational cost. Thus, it has been identified that the most significant parameter affecting BTMS efficiency is the battery space (h_b), and the structure width (W_c) as key design variables (DV), as shown in Figure 2. The ranges of the DVs are taken as: $3\text{mm} \leq h_b \leq 10\text{mm}$ and $5\text{mm} \leq W_c \leq 15\text{mm}$. Therefore, OLHS is selected for this study to generate 35 design of experiments (DOE) points. Figure 5 shows the uniform distribution of design variables (h_b, W_c) within the design space. Data summarising the 35 CFD simulation results are presented in Table 6 in Appendix A.

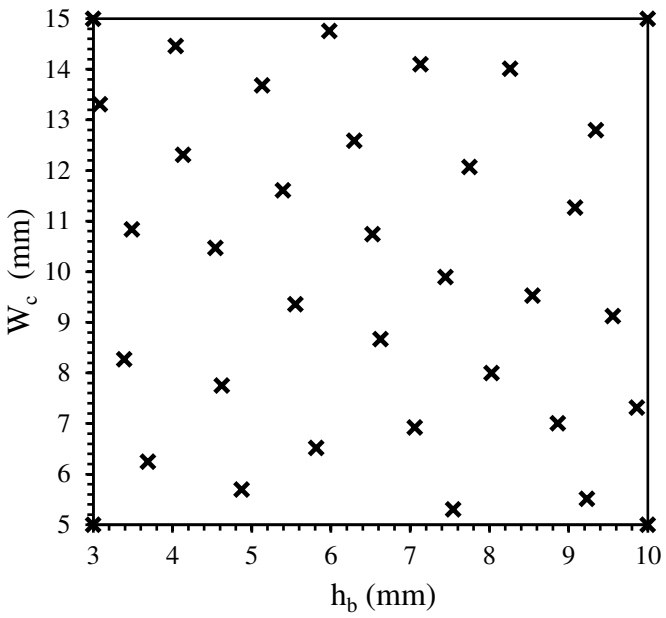

Fig. 5 DOE points distribution across the battery dimensions' space vs inlet/outlet width (see Figure 2).

3.2 Support Vector Regression

Support Vector Regression (SVR) is considered the subset of Support Vector Machine (SVM) applied to regression prediction tasks in machine learning. Technique of support vector machine relies on methodology of statistical learning. It works by finding the best balance of hyperplane that segregate the dataset into classes, mathematically the decision boundary (hyperplane) can be expressed by equation 18 [52]. Application of SVM for regression predication and function fitting tasks is known as SVR [53]. SVR can settle non-linear and complex correlations in data between input and objectives by utilising a function of Radial Basis Function (RBF). The main aim of SVR is to find the wight vector (w) and bias term (b), which minimises the loss functions while preserving a boundary of ϵ-intensive loss around the decision boundary [52]. The loss function can be calculated as expressed in equation 19.

$$f(x) = \omega . x + b, \tag{18}$$

$$\text{Minimise } \left[\frac{1}{2}\|\omega\|^2 + C \sum_{i=1}^{N} (\xi_i + \xi_i^*), \right. \tag{19}$$

Where, $f(x), \omega, x, b$ are the regression function, weight vector (uses to define the orientation of hyperplane), input feature vector, and bias term (uses to shift the hyperplane), respectively. $C, \xi_i, and\ \xi_i^*$ are regularisation parameter and slack variables. N is the DOE site.

Leave-one-out cross validation (LOOCV) is utilised to identify the optimum kernel functions. Radial Basis Function (RBF) is considered as an optimum kernel function due to effectively handling complex input data and helping to introduce non-linearity in the model. To evaluate the surrogate model performance, assessment metric is employed: root mean square error (RMSE) [54], expressed as follows:

$$\text{RMSE} = \sqrt{\frac{\sum[X_{\ predicted} - X]^2}{n}}. \tag{20}$$

3.3 Multi-Objective Design Optimisation

Multi-objective optimisation is executed to obtain the optimal design configuration by using Pareto fronts based on SVR and Generalized Differential Evolutionary Algorithm (GDE3). GDE3 is characterized by its elitist non-dominated sorting technique, significantly reducing computational requirements by employing a highly effective sorting algorithm [55]. The primary aim of GDE3 is to identify the optimal candidate points from Pareto that reduces the target objectives: pressure drop, maximum temperature, and temperature variation. The Pareto front comprises of a collection of feasible other solutions that demonstrate distinct trade-offs, where enhancements in one objective

necessitate compromising at least one other objective [56]. The corresponding multi-objective optimisation formulation is to minimise the functions $f_1(\boldsymbol{x})$, $f_2(\boldsymbol{x})$ and $f_3(\boldsymbol{x})$ defined as:

$$\left\{\begin{array}{lll} f_1(\boldsymbol{x}) = & \Delta p & (Pa) \\ f_2(\boldsymbol{x}) = & T_{\max} & (^oC) \\ f_3(\boldsymbol{x}) = & T_{diff} & (^oC) \end{array}\right\}. \tag{21}$$

with $\boldsymbol{x} = [h_b, W_c]$ and $[h_b, W_c] \in [3,\ 10] \times [5,\ 15]$.

The parameters set for GDE3 are listed in the following Table 8.

Table 8. GDE3 design parameters.

Parameter	Value
Population size	100
Maximum number of iterations	900
Crossover parameter (Cr)	0.8
Mutation parameter factor (F)	(0.0, 1.0)

4. Results

4.1 BTMS Immersion cooling performance at different discharge and flow rates

To optimize BTMS in Forced Flow Immersion Cooling (FFIC) applications, the study of influence of flow rates and discharge rates on cooling performance are conducted. The baseline model for this study was set at 25℃ ambient temperature with the battery space module of 5mm and structure width of 10 mm. Palm biodiesel is used as a coolant to be investigated. It is circulated through the battery module in a serpentine method as depicted in Figure 8, absorbing the heat generated during operating conditions. The objective of this section is to investigate the impact of different cases of 3S2P battery module and then use the findings in the design optimisation of BTMS.

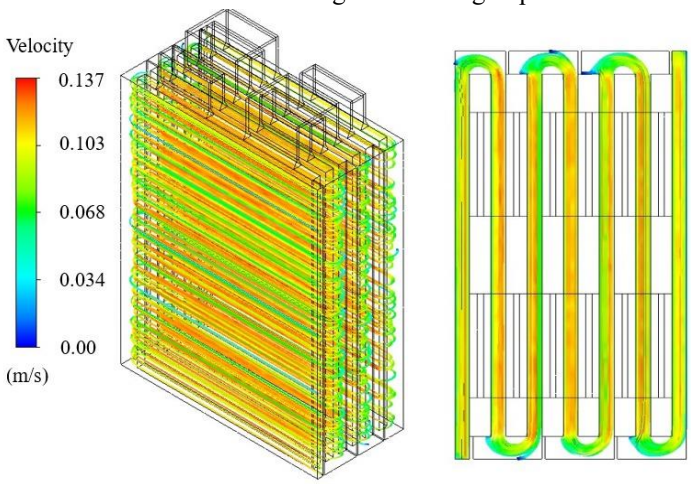

Fig. 8 Velocity streamlines of 3S2P battery module at 3C discharge rate and coolant flow rate of 0.09 m/s

Figure 9 illustrates the temperature distribution across the battery cells at 5C-rate and 0.05 m/s. For all cases, the highest temperature was observed in the cells 5 and 6 due to a flow stream approach of coolant that would carry heat from previous cells, as illustrated in Figure 8. However, it remained within a safe range and was comparable with other cells. This result suggests that in case of larger number of cells in a single module, a higher fluid flow rate or alternative cooling paths may need to be considered to maintain uniform temperature distribution.

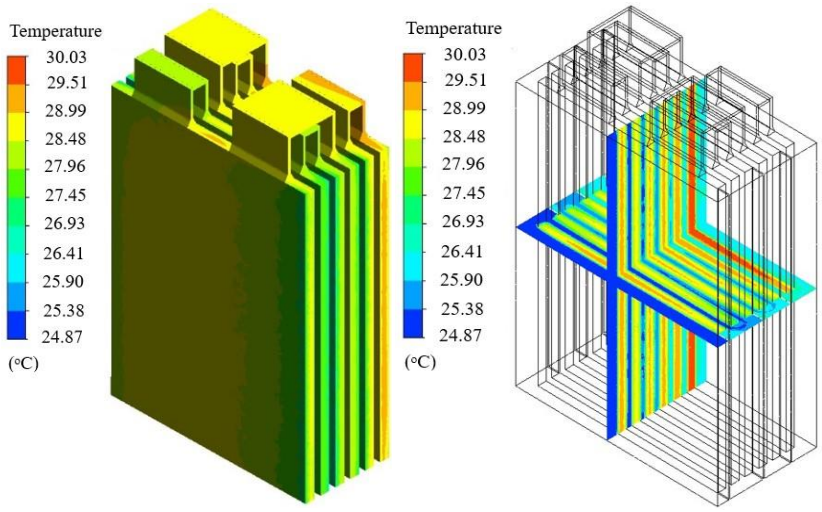

Fig. 9 Temperature distribution of 3S2P battery module at 5C discharge rate and 0.05 m/s fluid flow rate

Fluid flow rate is directly associated with power consumption through coolant pumping loses, depending on the heat generation within the cells, this can either increase or decrease. While the discharge current of Li-ion battery does not affect the pressure drop, even at high C-rate. Although battery maximum temperature and temperature variation varied along with different discharge currents, pressure drop remained the same and only varied because of changing velocity, as referred to in Table 9. As inlet velocity increased from 0.01 m/s to 0.09 m/s, the pressure drop increased from 32.676 Pa to 386.813 Pa, while the battery maximum temperature remained within the operational threshold (<40°C) for all cases. In addition, the power consumption would be increased due to the high viscosity of the palm biodiesel coolant. Therefore, based on the results in Table 9, the direct fluid inlet velocity of 0.05 m/s and 5C-rate could be selected to optimise the BTMS, resulting in preserving the battery maximum temperature and temperature variation below 40°C and 5°C, respectively, and presenting a moderate pressure drop to minimise power consumption.

Table 9. Maximum battery temperature, temperature variation, and pressure drop at different C-rates

C-rate	Fluid Velocity (m/s)	Maximum Temperature °C	Temperature difference °C	Pressure drops (Pa)
2C	0.01	27.454	1.91	32.676
	0.05	26.074	0.871	185.61
	0.09	25.844	0.702	386.79
3C	0.01	29.835	3.664	32.676
	0.05	27.2	1.769	185.61
	0.09	26.742	1.442	386.61
5C	0.01	35.55	7.74	32.676
	0.05	30.1	4	185.61
	0.09	29.08	3.35	386.813

4.2 Comparative analysis and validation

Validation of the computational model with experimental work is essential to ensure the reliability of the numerical work. The validation of the single battery heat generation is performed well against the experimental work. And the qualitative validation of BTMS-based immersion cooling using biodiesel as coolant is carried out, by comparing the thermal performance against well-established findings from the literature, to evaluate the cooling effectiveness of the designed direct cooling (biodiesel-Palm) along with another immersion cooling and indirect liquid cooling.

4.2.1 Single cell

To validate thermal behaviour numerical model without BTMS, transient single battery cell is compared with experimental results obtained by Patil et al., [31]. Figure 6 shows maximum temperature profile of pouch battery single cell (20 Ah $LiFeO_4$) at 3C discharge rate, alongside with thermal imaging captured upon completion of the discharge process. Comparison results illustrated that developed numerical model has a good accuracy and agreement. Although, due to its complexity, not all physical phenomena occurring in the battery call has been captured however, the numerical model is accurate enough to conduct this study with confidence. It is worth to note that the maximum temperature exceeded 40 ℃ above ambient temperature, which might lead to a significant risk. Therefore, an effective BTMS is necessary to minimise such thermal conditions and ensure safe operation of battery modules and packs based on such cells.

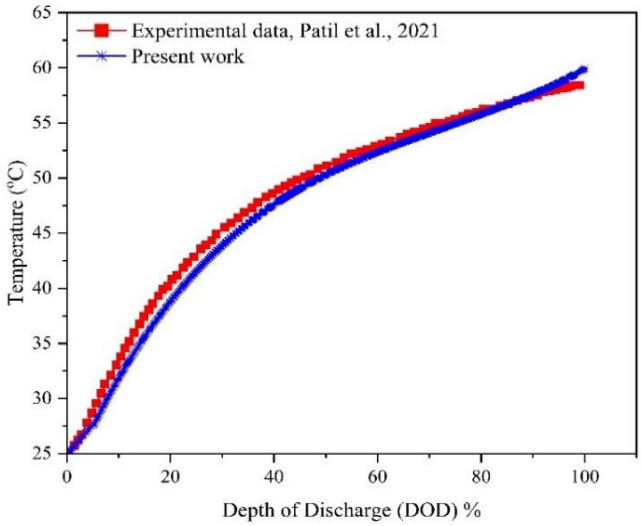

Fig. 6 Numerical validation: Comparison with experimental results for 20 Ah at 3C-rate [31]

Furthermore, another validation of battery heat generation is conducted based on a high discharge C-rate at 5C. The C-rate refers to charging/discharge battery current relative to its nominal cell capacity. Sheng et al. [57] investigated an experimental study to evaluate the heat generation rate of battery cell (8 Ah, $LiFePO_4$) at 5C-dicharge rate and ambient temperature of 30 ℃.

Consequently, a single battery cell without BTMS is compared with experimental results obtained by Sheng et al., [57] to validate the numerical model. Figure 7 depicts the temperature difference of a battery cell at 5C-discharge rate (8 Ah, $LiFePO_4$). The simulation result demonstrates good agreement with experimental results and illustrates accuracy of developed numerical model in this work at high discharge rate. Here also it is significant to note that the maximum temperature exceeded the temperature limit (40℃), which can highlight a significant risk. This observation emphasises need for an effective BTMS to minimise the thermal challenges.

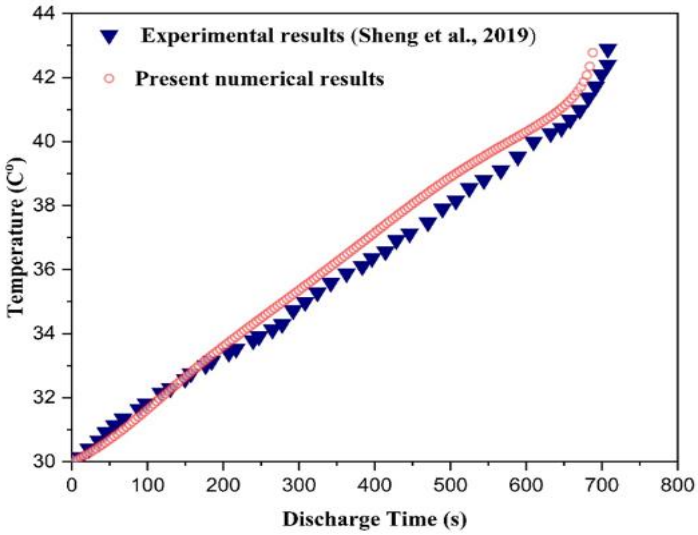

Fig. 7 Numerical validation: Comparison with experimental results for 8 Ah at 5C-rate [57].

4.2.2 Battery module

Palm biodiesel coolant shows superior cooling performance to mineral oil and water-glycol, particularly at low inlet flow rate. The effectiveness of its thermophysical properties, including high thermal conductivity and lower density, makes it well-suited for BTMS applications. To understand and evaluate our analysis, the present numerical study was compared with two different BTMS design. The first one used a mini-channel cold plate using water-glycol as a coolant and a prismatic cell (20Ah) at (3C & 5C-rate) discharge rate and 0.05 m/s, obtained by [58]. The second study used immersion cooling with tab cooling and the battery cell was a pouch (20 Ah) at (3C & 5C) discharge rate and 0.077 kg/s mass flow rate, obtained by [31]. 3S2P battery module using palm biodiesel as a coolant reduces the maximum temperature at 3C-rate by approximately 11.6 % and 8.4 %, compared to Li et al. [58] and Patil et al. [31], respectively, as shown in Figure 10-(a). While at 5C-rate it is minimized by 24.88 % and 17.89 % compared to the obtained results, correspondingly, as depicted in Figure 10-(b). Therefore, biodiesel coolants, particularly palm oil, offer enhance cooling efficiency at low inlet velocities and fulfil lower temperatures compared to mineral oil and mini-channel cold plate. Also, it achieved lower temperatures variation compared to air and 3M-Novec 7100 as stated in our previous study [21].

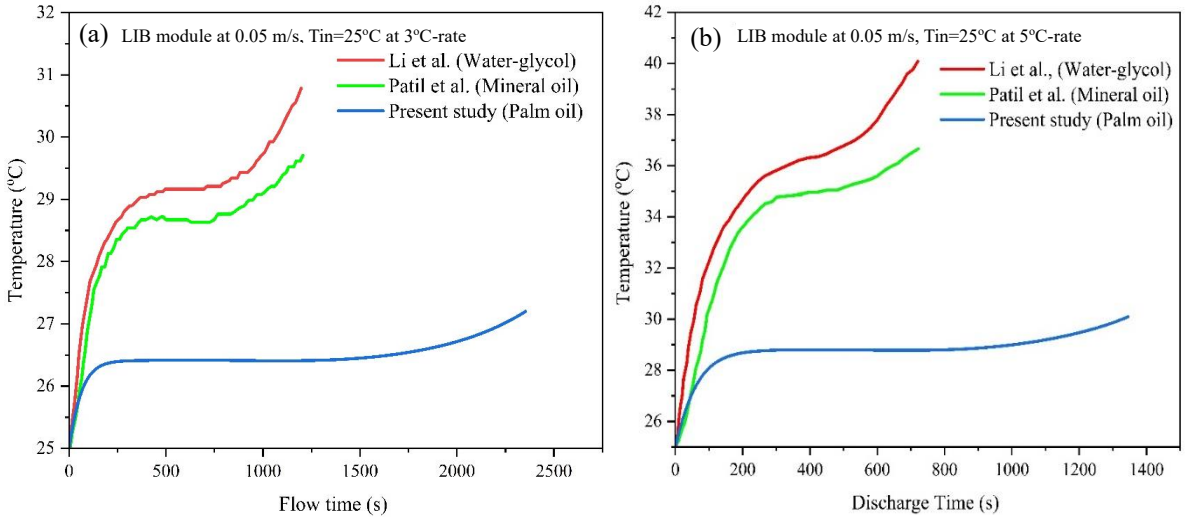

Fig. 10 3S2P battery module maximum temperature comparison with mini-channel cold plate [58] and immersion cooling [31] (a) at 3C-rate, and (b) at 5C-rate

As stated earlier in Section 2.2, the discharge time is slower compared to the obtained results due to the configuration of the battery module four cells in series and two cells in parallel connection, leading to an increase in the capacity of a module, which significantly contributed to slowing down the discharge time. The battery heat generation rate at the beginning of discharge generally increases. Hence, from 0% DOD to around 10% DOD, heat generation increased sharply, then there was a stability in heat generation until it reached 85% of DOD the heat generation increased towards the end of discharge. This behaviour of battery heat generation is aligned with results from existing literature [59, 60, 61].

4.3 Sensitivity analysis

The optimisation study initiates with a robust single-factor analysis, systematically adjusting each input variable based on the baseline solution. This method enables a comprehensive exploration of how design variable parameters significantly impact optimisation objectives. The design variables and their corresponding value ranges are detailed in Table 10, while the calculation results are depicted in Figure 11.

Table 10. Cases of design variables

Name	Description	W_c (mm)	h_b (mm)	C-rate	Flow velocity (m/s)
Single factor analysis	Varying structural width	5 to 15	5	5	0.05
	Varying battery spacing	3 to 10	10	5	0.05
Optimisation	Multi-objective optimisation	5 to 15	3 to 10	5	0.05

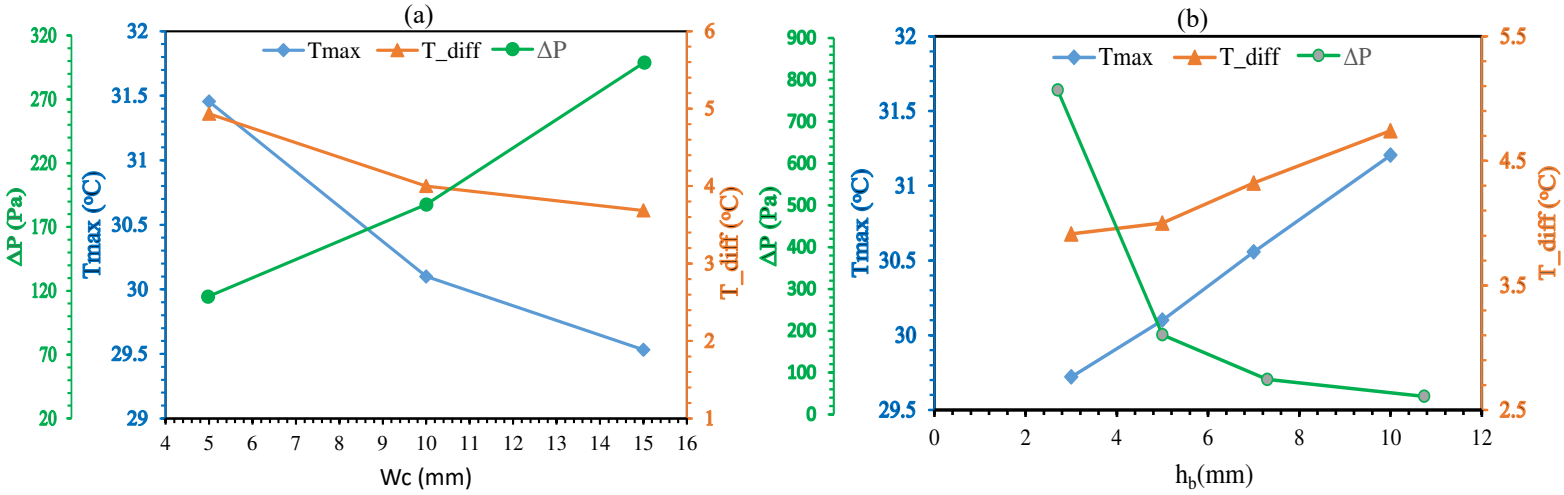

Fig. 11 Single factor analysis for T_{max}, T_{diff}, and ΔP at 5C-rate and 0.05m/s: (a) W_c, (b) h_b

Figure 11 (a) illustrates the impact of structural inlet/outlet width (W_c) on the thermal performance and power consumption. As the Wc increases, the maximum temperature of battery module decreases, along with a slight reduction in the temperature difference. However, this benefit comes at a cost; the pressure drop escalates significantly with a wider structural design, adversely affecting energy efficiency. This clearly demonstrates that structural width plays a vital role in determining the temperature dynamics of the battery module and the associated pressure drop.

Figure 11 (b) further examines the effect of battery spacing (h_b) on the three key objectives. As the h_b increases, the thermal performance of the battery module declines, although both T_{max}, and T_{diff} remain within the operating temperature limits. Notably, a smaller battery spacing markedly improves thermal performance, but this advantage is offset by a heightened pressure drop, which can significantly compromise overall power consumption.

Consequently, to optimize the balance among the three objectives—T_{max}, T_{diff}, and ΔP—strategic trade-offs are essential. Employing Multi-Objective Optimization (MOO) becomes imperative for achieving superior thermal

performance of the battery module while simultaneously minimizing power consumption. This balanced approach is key to maximizing efficiency and sustainability in battery systems.

4.4 Multi-Objective Optimisation

Generalised differential evolutionary algorithm (GDE3) is used to generate Pareto fronts by using SVR metamodeling, which is available in the pymoo Python package. GDE3 outperformed several optimisation algorithms in terms of accuracy, leading for the optimisation study [24]. An RBF is implemented to generate metamodels for T_{max}, T_{diff}, and ΔP using LOOCV approach. The coefficient of determination (R^2) is a pivotal metric for evaluating the predictive ability of a support vector regression surrogate model. It effectively quantifies the alignment between the model's predictions and the actual values, with a range stretching from 0 to 1. A higher R^2 significantly indicates superior model performance. Remarkably, all R^2 values in this analysis exceed 0.9, highlighting a strong correlation between the actual and predicted results, and demonstrating the robustness of the metamodel.

While the surrogate models developed using Support Vector Regression (SVR) and Radial Basis Function (RBF) kernels demonstrated excellent agreement with CFD results within the defined design space ($R^2 > 0.99$ and <3% error), it is important to acknowledge potential limitations in extrapolation beyond the sampled domain. The 35 DOE points generated via Optimal Latin Hypercube Sampling (OLHS) provide a well-distributed representation of the design space, e.g. Figure 5 in Section 3.1; however, regions with steep gradients or nonlinear interactions may require denser sampling to maintain predictive accuracy. Future work could incorporate adaptive sampling strategies or active learning techniques to refine the surrogate model in high-sensitivity regions. This would enhance the model's robustness and generalisability, particularly for applications involving dynamic operating conditions or extended geometric configurations.

Figure 12 demonstrates the metamodeling process validity of the predicated models, which are used to evaluate the predication performance. This indicates that SVR metamodels accurately predict T_{max}, T_{diff}, and ΔP.

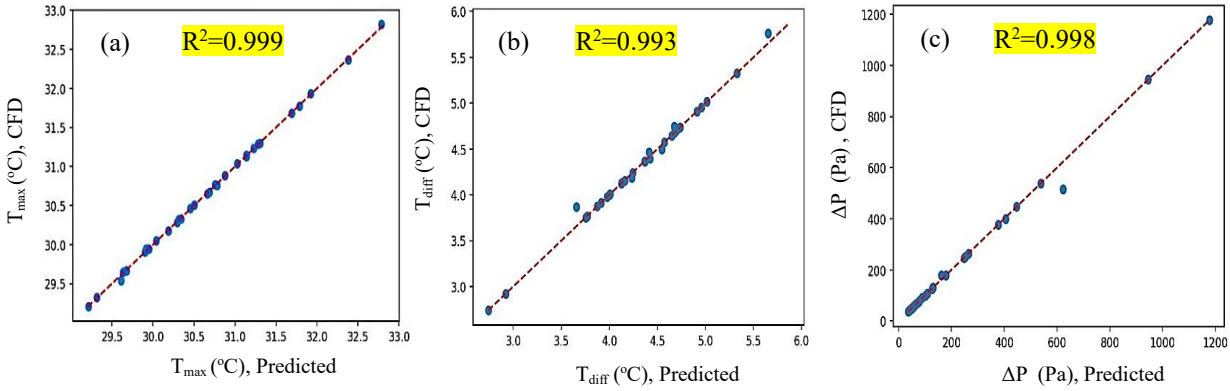

Fig. 12 Metamodeling validation: comparison of the metamodel predictions with the CFD numerical solutions for (a) T_{max}, (b) T_{diff}, and (c) ΔP

Figure 13 displays the Pareto front representing the compromise between the battery maximum temperature and pressure drop. The data reveal that any decrease of T_{max} is followed by an increase of ΔP.

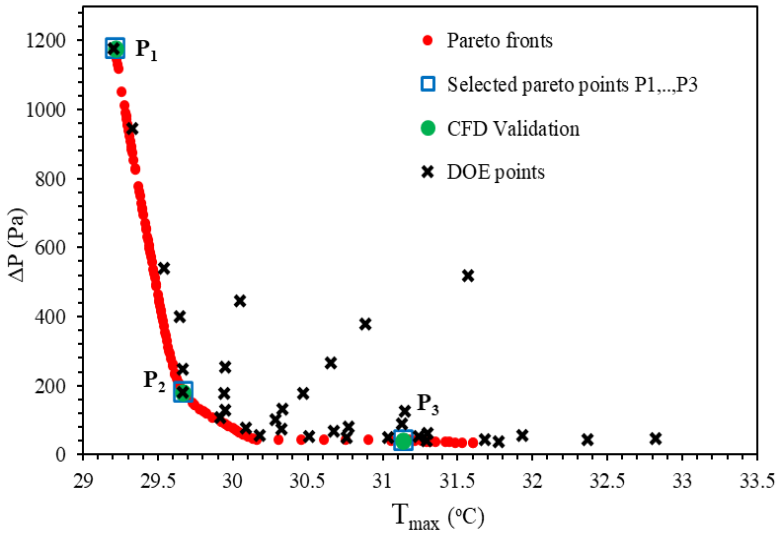

Fig. 13 Pareto fronts curve of T_{max} vs. ΔP using the SVR approach together with the DOE points

Table 11 lists three points on the Pareto front together with of the metamodel validation with CFD results, demonstrating the accuracy of the surrogate modelling framework developed. An excellent agreement is observed between the surrogate models and the numerical simulations, with a percentage error being <3.5% for all cases.

Table 11. Design performance of BMTS at three operating condition points located on the Pareto front together with CFD validation.

Points	Design Variables		T_{max}		Pressure		% Error	
	h_b *(mm)*	W_c *(mm)*	Metamodel	CFD	Metamodel	CFD	T_{max}	Pressure
P1	3	14.999	29.215	29.215	1177.14	1177.14	0	0
P2	6.005	14.954	29.67	29.668	181.459	180.216	0.0067	0.685
P3	9.613	9.939	31.137	31.134	42.546	41.042	0.009	3.535

Figure 14 demonstrates the Pareto front of maximum temperature and temperature variation. The differences in the battery temperature are minimal as shown, attributed to the high linearity observed between two objectives: T_{max} and T_{diff}.

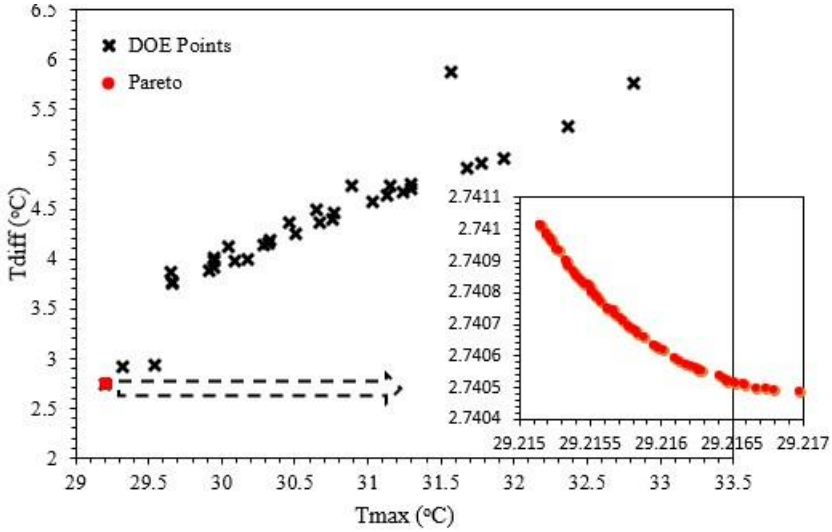

Fig. 14 Pareto front curve of T_{max} vs. T_{diff} using the SVR approach together with the DOE points

Figure 15 presents the Pareto front between T_{diff} against ΔP. Here again, a pressure drop increase yields a decrease in the temperature variation of the battery module. The optimisation results revealed that BTMS designers can judge the balance between competing targets. For example, to minimize the battery maximum temperature from 31.6 ºC to 29.2 ºC would require more power and a ensuing pressure drop increase from 35.58 Pa to 1177 Pa, as shown in Figure 12.

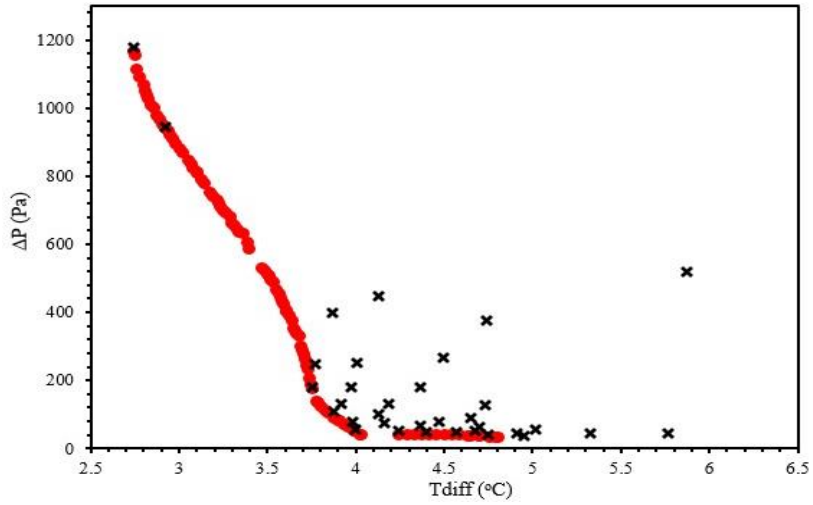

Fig. 15 Pareto fronts curve of T_{diff} vs. ΔP using the SVR approach together with the DOE points

Finally, Figure 16 displays a 3D Pareto surface representation emphasising the compromise that can be met between the three objectives T_{max}, T_{diff}, and ΔP.

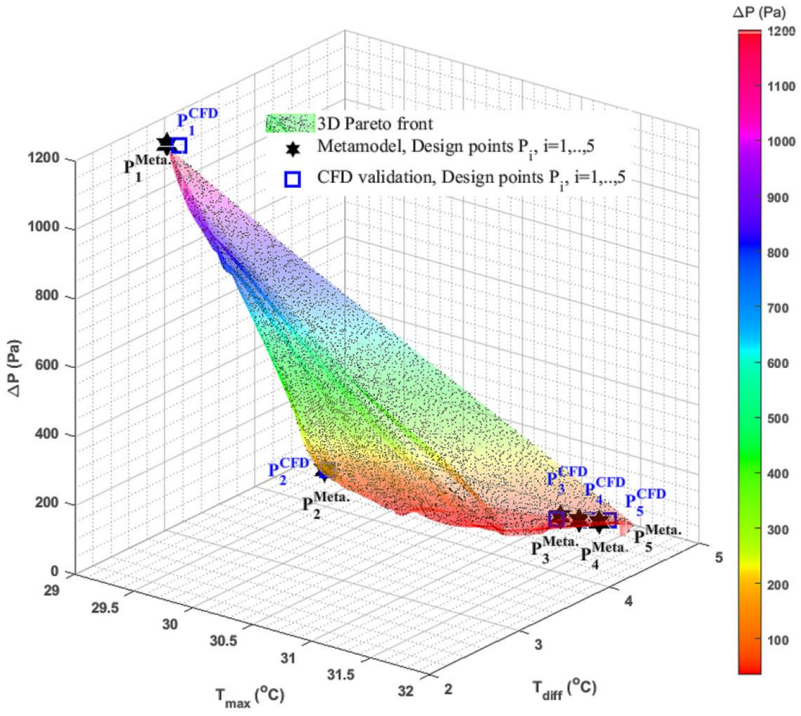

Fig. 16 3D Pareto surface together with metamodel predictions and corresponding CFD validations at five design points as defined in Table 10.

The Pareto fronts generated in this study reveal critical trade-offs between maximum temperature, temperature uniformity, and pressure drop — each of which carries distinct engineering implications depending on the application context. For instance, in electric vehicle (EV) applications where energy efficiency and range are paramount, designers may prioritise lower pressure drop to minimise pumping power and extend battery life. Conversely, in stationary

energy storage systems, where thermal stability and safety are more critical than energy efficiency, temperature uniformity may take precedence to prevent localised overheating and extend module lifespan. The flexibility of the GDE3 optimisation framework allows engineers to select design points that best align with their operational priorities, whether that be minimising energy consumption, enhancing safety, or balancing both. This adaptability makes the proposed framework highly applicable across diverse BTMS deployment scenarios.

The accuracy of the optimisation framework developed is evidenced through five design points, P_1,.., P_5 on the Pareto where metamodel and CFD results are displayed, and compare very well. This is further demonstrated in Table 12, where the percentage error between the metamodel predictions and CFD calculations is less than 3% overall.

Table 12. Design performance of BMTS at four design points located on the Pareto together with CFD validations.

Desing Points #	Design variables		T_{max} (°C)		T_{diff} (°C)		ΔP (Pa)		% Error		
	h_b (mm)	W_c (mm)	Metamodel	CFD	Metamodel	CFD	Metamodel	CFD	T_{max}	T_{diff}	Pressure
P_1	3	14.987	29.215	29.3	2.74	2.768	1176.355	1178.072	0.29	1.02	0.146
P_2	6.523	14.993	29.742	29.758	3.799	3.81	145.275	146.166	0.0538	0.289	0.613
P_3	9.891	8.865	31.371	31.406	4.711	4.767	37.054	37.18	0.11	0.11	0.34
P_4	9.993	9.503	31.256	31.302	4.639	4.683	39.483	38.349	0.147	0.948	2.871
P_5	9.433	9.857	31.129	31.131	4.598	4.553	42.902	42.181	0.0064	0.979	1.68

Compromise design point is selected among other non-dominated solutions and is placed in the left corner of the Pareto surface, e.g. design point P_2 in Table 12. The compromise design point shows superior upgrades compared to benchmark results. There is a minimisation in three target objectives (i.e., T_{max}, T_{diff}, and ΔP) by 1.19 %, 5.8 %, and 21.73 %, respectively. The maximum temperature reduced from 30.1 °C to 29.74 °C, while the temperature variation and pressure drop decreased from 4 °C to 3.768 °C and 185.61 Pa to 145.275 Pa, correspondingly, as shown Table 13.

In addition, the design point indicates that the maximum temperature is reduced by 25.789 % compared to the mini-channel cold plate and by 18.876 % compared to mineral oil immersion cooling. Therefore, the optimisation framework improves the percentage reduction of the battery's maximum temperature, increasing it from 24.789 % to 25.789 % and from 17.89 % to 18.876 %, respectively. Eventually, decision making on which design is best appropriate will depend on various factors such as manufacturing capability, applications and other engineering constraints.

Table 13: Candidate design point compared to benchmark results.

	Acronym	Benchmark Design	Optimum Candidate Design
Design Variables	h_b (mm)	5	6.523
	W_c (mm)	10	14.993
Objectives Functions	T_{max} (°C)	30.1	29.742
	T_{diff} (°C)	4	3.799
	ΔP (Pa)	185.61	145.275

5. Conclusion

In this study, a new numerical model of heat generation during a discharge process was developed for $LiFePO_4$ battery pouch cell. It was validated against published experimental data for up to 5C discharge rate. For the first time, an optimisation methodology for battery thermal management systems (BTMSs) immersion cooling is laid out which combines Support Vector Regression (SVR) and Generalized Differential Evolutionary Algorithm (GDE3). A robust functional relationship between critical design parameter (i.e, battery space and inlet/outlet width) is established, and allowing appropriate key operating conditions, including maximum temperature, temperature differential, and pressure drop. With introduction of GDE3 algorithm within the framework, a comprehensive three-dimensional Pareto

surface was generated, enabling a detailed analysis of compromises among three key objectives and facilitating the identification of optimal design points. This thorough evaluation ultimately enhances the cooling performance of BTMS, paving the way for more efficient and effective solutions in battery management. The key findings are concluded as follows:

- Through CFD-driven optimisation of a 3S2P pouch cell module (20 Ah $LiFePO_4$), biodiesel demonstrated exceptional thermal regulation - maintaining maximum temperatures below 29.9°C at 5C discharge rates and limiting cell-to-cell variations to $\Delta T < 5°C$.
- The integrated framework, combining Newman, Tiedemann, Gu, and Kim (NTGK) electrochemical modelling, conjugate heat transfer simulation, and surrogate-assisted multi-objective optimisation, provides a replicable template for BTMS design. Optimal Latin Hypercube Sampling (OLHS) efficiently navigated complex parameter interactions, while SVR with RBF kernels achieved high prediction accuracy. This approach demonstrates how computational methods can accelerate sustainable thermal solutions development and design.
- The optimised system geometry (5 mm battery gap, 10 mm inlet width) at 0.05 m/s and 5C-rate and selected the candidate point 1 achieved an optimal balance between thermal homogeneity and hydraulic efficiency, which reduced the maximum temperature by 1.19 % (30.1 ºC to 29.742 ºC), the temperature difference by 5.8 % (4 ºC to 3.799 ºC), and the pressure drop 21.73 % (185.61 Pa to 145.275 Pa). In addition, it represents 25.789 % improvements over the conventional mini-channel cold plate and a 18.876 % enhancement versus mineral oil immersion cooling.
- Beyond thermal performance, palm biodiesel offers critical sustainability advantages: a 43% reduction in system weight versus systems that use fluorinated coolants, and >80% cost savings ($4–7/L vs. $50–100/L for 3M-Novec 7100). Its biodegradability and non-toxic profile further address lifecycle environmental concerns absent in synthetic alternatives. The GDE3 optimized design eliminates thermal runaway risks while enabling lighter, more energy-dense battery packs—directly supporting electric vehicle range extension.

In summary, the work presents a novel palm biodiesel optimisation of BTMS immersion cooling, and SVR machine learning approach within multi-objective optimisation using GDE3. By using biodiesel as a viable coolant, the cooling performance of the BTMS was thoroughly evaluated. In addition, it significantly contributes to achieving weight reduction of the filled enclosure, which would improve the system performance. In the future work, battery module could be conducted to validate BTMS-based optimised performance in real world scenario. In addition, driving cycle and battery under thermal runway might also be considered within an optimisation framework.

References

[1] C. Roe *et al.*, “Immersion cooling for lithium-ion batteries – A review,” Mar. 30, 2022, *Elsevier B.V.* doi: 10.1016/j.jpowsour.2022.231094.

[2] E. Fan *et al.*, “Sustainable Recycling Technology for Li-Ion Batteries and Beyond: Challenges and Future Prospects,” Jul. 22, 2020, *American Chemical Society*. doi: 10.1021/acs.chemrev.9b00535.

[3] H. Fayaz *et al.*, “Optimization of Thermal and Structural Design in Lithium-Ion Batteries to Obtain Energy Efficient Battery Thermal Management System (BTMS): A Critical Review,” Jan. 01, 2022, *Springer Science and Business Media B.V.* doi: 10.1007/s11831-021-09571-0.

[4] S. Du *et al.*, “An investigation of irreversible heat generation in lithium ion batteries based on a thermo-electrochemical coupling method,” *Appl Therm Eng*, vol. 121, pp. 501–510, 2017, doi: 10.1016/j.applthermaleng.2017.04.077.

[5] Z. Esmaeili, S. M. Vahidhosseini, S. Rashidi, N. Karimi, and W. M. Yan, “Thermal management of lithium-ion batteries: Numerical evaluation of phase change materials and fin designs against air cooling,” *International Journal of Thermal Sciences*, vol. 219, Jan. 2026, doi: 10.1016/j.ijthermalsci.2025.110194.

[6] P. M. Sutheesh, N. R. Bandi, and R. Bandaru, “Thermal performance of Lithium-Ion battery pack with optimised bionic channel using Multi-Objective genetic Algorithm: A numerical Investigation,” *Thermal Science and Engineering Progress*, vol. 60, Apr. 2025, doi: 10.1016/j.tsep.2025.103414.

[7] H. Ammar *et al.*, “Hybrid liquid–PCM thermal management for high–capacity lithium–ion batteries under fast charging: A parametric comparative study,” *Results in Engineering*, vol. 27, Sep. 2025, doi: 10.1016/j.rineng.2025.106674.

[8] Y. Liu and J. Zhang, “Self-adapting J-type air-based battery thermal management system via model predictive control,” *Appl Energy*, vol. 263, Apr. 2020, doi: 10.1016/j.apenergy.2020.114640.

[9] P. Qin, M. Liao, D. Zhang, Y. Liu, J. Sun, and Q. Wang, “Experimental and numerical study on a novel hybrid battery thermal management system integrated forced-air convection and phase change material,” *Energy Convers Manag*, vol. 195, pp. 1371–1381, Sep. 2019, doi: 10.1016/j.enconman.2019.05.084.

[10] M. S. Patil, J. H. Seo, S. Panchal, and M. Y. Lee, “Numerical study on sensitivity analysis of factors influencing liquid cooling with double cold-plate for lithium-ion pouch cell,” *Int J Energy Res*, vol. 45, no. 2, pp. 2533–2559, Feb. 2021, doi: 10.1002/er.5946.

[11] D. W. Sundin and S. Sponholtz, “Thermal management of Li-ion batteries with single-phase liquid immersion cooling,” *IEEE Open Journal of Vehicular Technology*, vol. 1, pp. 82–92, 2020, doi: 10.1109/OJVT.2020.2972541.

[12] “Comparison of lumped and 1D electrochemical models for prismatic 20Ah LiFePO4 battery sandwich between minichannel”.

[13] C. Akkaldevi, S. D. Chitta, J. Jaidi, S. Panchal, M. Fowler, and R. Fraser, “Coupled Electrochemical-Thermal Simulations and Validation of Minichannel Cold-Plate Water-Cooled Prismatic 20 Ah LiFePO4 Battery,” *Electrochem*, vol. 2, no. 4, pp. 643–663, Dec. 2021, doi: 10.3390/electrochem2040040.

[14] J. Kim, J. Oh, and H. Lee, “Review on battery thermal managemnt system for electric vehicles,” *Appl Therm Eng*, no. 149, pp. 192–212, Dec. 2019, doi: https://doi.org/10.1016/j.applthermaleng.2018.12.020.

[15] H. Hu, J. Xu, J. Li, and H. Xi, “Immersion coupled direct cooling with non-uniform cooling pipes for efficient lithium-ion battery thermal management,” *J Energy Storage*, vol. 116, Apr. 2025, doi: 10.1016/j.est.2025.116010.

[16] M. Al Qubeissi, A. Almshahy, A. Mahmoud, M. T. Al-Asadi, and R. M. A. Shah, "Modelling of battery thermal management: A new concept of cooling using fuel," *Fuel*, vol. 310, 2022, doi: 10.1016/j.fuel.2021.122403.

[17] M. Al Qubeissi, R. M. R. A. Shah, and A. Almshahy, "Battery thermal management using heavy fuels: An approach to lightweight diesel fuelled hybrid electric vehicles," *Alexandria Engineering Journal*, vol. 126, pp. 515–545, Jul. 2025, doi: 10.1016/j.aej.2025.04.064.

[18] Z. Zhu, Z. Zhang, Z. Kuang, W. Qin, and C. Yin, "Multi-objective optimization of immersion cooling system for large-capacity lithium-ion battery with collaborative thermal management structures," *Energy*, vol. 328, Aug. 2025, doi: 10.1016/j.energy.2025.136561.

[19] A. Adeniran, J. Bak, B. Bhatia, and S. Park, "Optimizing single-phase immersion cooling system for lithium-ion battery modules in electric vehicles: A multi-objective design approach," *International Journal of Thermal Sciences*, vol. 210, Apr. 2025, doi: 10.1016/j.ijthermalsci.2024.109636.

[20] Z. Guo, J. Xu, Z. Xu, M. Mubashir, H. Wang, and X. Mei, "A Lightweight Multichannel Direct Contact Liquid-Cooling System and Its Optimization for Lithium-Ion Batteries," *IEEE Transactions on Transportation Electrification*, vol. 8, no. 2, pp. 2334–2345, Jun. 2022, doi: 10.1109/TTE.2021.3131718.

[21] M. Al Qubeissi *et al.*, "Comparative Analysis of Battery Thermal Management System Using Biodiesel Fuels," *Energies (Basel)*, vol. 16, no. 1, 2023, doi: 10.3390/en16010565.

[22] S. Wankhede, K. More, and L. Kamble, "A review of Li-ion battery temperature control and a key future perspective on cutting-edge cooling methods for electrical vehicle applications," Feb. 01, 2024, *John Wiley and Sons Inc*. doi: 10.1002/est2.572.

[23] S. Kukkonen and J. Lampinen, "GDE3: The third Evolution Step of Generalized Differential Evolution."

[24] B. Leite, A. O. S. da Costa, and E. F. da Costa Junior, "Multi-objective optimization of adiabatic styrene reactors using Generalized Differential Evolution 3 (GDE3)," *Chem Eng Sci*, vol. 265, Jan. 2023, doi: 10.1016/j.ces.2022.118196.

[25] Y. Li, C. Li, A. Garg, L. Gao, and W. Li, "Heat dissipation analysis and multi-objective optimization of a permanent magnet synchronous motor using surrogate assisted method," *Case Studies in Thermal Engineering*, vol. 27, Oct. 2021, doi: 10.1016/j.csite.2021.101203.

[26] X. Zhang, Z. Li, L. Luo, Y. Fan, and Z. Du, "A review on thermal management of lithium-ion batteries for electric vehicles," *Energy*, vol. 238, Jan. 2022, doi: 10.1016/j.energy.2021.121652.

[27] S. Wankhede, A. Kore, L. Kamble, and P. Kale, "Experimental investigation on an innovative serpentine channel-based nanofluid cooling technology for modular lithium-ion battery thermal management," *Heat Transfer*, Dec. 2024, doi: 10.1002/htj.23156.

[28] S. Wankhede, A. D. Pingale, and A. Kale, "Experimental investigation on thermal management of lithium-ion battery pack for formula student electric vehicle using air-cooling system," *Energy Storage and Saving*, vol. 4, no. 1, pp. 38–47, Mar. 2025, doi: 10.1016/j.enss.2024.11.008.

[29] V. Mali, R. Saxena, K. Kumar, A. Kalam, and B. Tripathi, "Review on battery thermal management systems for energy-efficient electric vehicles," Nov. 01, 2021, *Elsevier Ltd*. doi: 10.1016/j.rser.2021.111611.

[30] R. Kumar and V. Goel, "A study on thermal management system of lithium-ion batteries for electrical vehicles: A critical review," Nov. 01, 2023, *Elsevier Ltd*. doi: 10.1016/j.est.2023.108025.

[31] M. S. Patil, J.-H. Seo, and M.-Y. Lee, "A novel dielectric fluid immersion cooling technology for Li-ion battery thermal managment," *Energy Convers Manag*, vol. 229, p. 113, Dec. 2021.

[32] K. H. Kwon, C. B. Shin, T. H. Kang, and C.-S. Kim, “A two-dimensional modeling of a lithium-polymer battery,” *J Power Sources*, vol. 163, pp. 151–157, Apr. 2006.

[33] U. S. Kim, C. B. Shin, and C. S. Kim, “Modeling for the scale-up of a lithium-ion polymer battery,” *J Power Sources*, vol. 189, no. 1, pp. 841–846, Apr. 2009, doi: 10.1016/j.jpowsour.2008.10.019.

[34] Y. Liu, G. Aldan, X. Huang, and M. Hao, “Single-phase static immersion cooling for cylindrical lithium-ion battery module,” *Appl Therm Eng*, vol. 233, Oct. 2023, doi: 10.1016/j.applthermaleng.2023.121184.

[35] M. Donmez, M. Tekin, and M. I. Karamangil, “Artificial neural network predictions for temperature Utilizing numerical anaylsis in immersion cooling system using mineral oil and an engineered fluid for 32700,” *International Journal of Thermal Sciences*, vol. 211, pp. 109–742, Jan. 2025, doi: https://doi.org/10.1016/j.ijthermalsci.2025.109742.

[36] D. Kong, R. Peng, P. Ping, J. Du, G. Chen, and J. Wen, “A novel battery thermal management system coupling with PCM and optimized controllable liquid cooling for different ambient temperatures,” *Energy Convers Manag*, vol. 204, Jan. 2020, doi: 10.1016/j.enconman.2019.112280.

[37] R. Banerjee and K. Nidhul, “Effect of various dielectric fluids on temperature homogeneity of Li-ion battery pack in an energy efficient novel immersion cooling design,” *Results in Engineering*, vol. 26, Jun. 2025, doi: 10.1016/j.rineng.2025.104688.

[38] H. Wang, T. Tao, J. Xu, H. Shi, X. Mei, and P. Gou, “Thermal performance of a liquid-immersed battery thermal management system for li-ion pouch batteries,” *J Energy Storage*, vol. 46, p. 103, Dec. 2022, doi: https://doi.org/10.1016/j.est.2021.103835.

[39] S. J. Bazinski, X. Wang, B. P. Sangeorzan, and L. Guessous, “Measuring and assessing the effective in-plane thermal conductivity of lithium iron phosphate pouch cells,” *Energy*, vol. 114, pp. 1085–1092, Nov. 2016, doi: 10.1016/j.energy.2016.08.087.

[40] L. Wei *et al.*, “A comprehensive study on thermal conductivity of the lithium-ion battery,” *Int J Energy Res*, vol. 44, no. 12, pp. 9466–9478, Oct. 2020, doi: 10.1002/er.5016.

[41] J. W. Han, K. S. Garud, E. H. Kang, and M. Y. Lee, “Numerical Study on Heat Transfer Characteristics of Dielectric Fluid Immersion Cooling with Fin Structures for Lithium-Ion Batteries,” *Symmetry (Basel)*, vol. 15, no. 1, Jan. 2023, doi: 10.3390/sym15010092.

[42] M. H. Mat Yasin, R. Mamat, K. V. Sharma, and A. F. Yusop, “Influence of Palm Methyl Ester (PME) as an Alternative Fuel in Multicylinder Diesel Engine,” *JOURNAL OF MECHANICAL ENGINEERING AND SCIENCES*, vol. 3, pp. 331–339, Dec. 2012, doi: 10.15282/jmes.3.2012.9.0031.

[43] T. Mayer and E. Donzow, “Design of Battery Packs: Strategies for High Energy Density and Range,” 2019. doi: https://doi.org/10.1007/s38314-019-0095-4.

[44] P. E. Tuma, *Twenty Seventh Annual IEEE Semiconductor Thermal Measurement and Management Symposium : proceedings 2011 : San Jose, CA, USA : March 20-24, 2011*. IEEE, 2011. doi: https://doi.org/10.1109/STHERM.2011.5767224.

[45] Z. An, L. Jia, X. Li, and Y. Ding, “Experimental investigation on lithium-ion battery thermal management based on flow boiling in mini-channel,” *Appl Therm Eng*, vol. 117, pp. 534–543, 2017, doi: 10.1016/j.applthermaleng.2017.02.053.

[46] C. M. Barnes and P. E. Tuma, “Practical considerations relating to immersion cooling of power electronics in traction systems,” *IEEE Trans Power Electron*, vol. 25, no. 9, pp. 2478–2485, 2010, doi: 10.1109/TPEL.2010.2049864.

[47] 3M, "3M™ Novec™ 7000 Engineered Fluid Product Description," Sep. 2021. doi: https://multimedia.3m.com/mws/media/121372O/3m-novec-7000-engineered-fluid-tds.

[48] Y. F. Wang and J. T. Wu, "Thermal performance predictions for an HFE-7000 direct flow boiling cooled battery thermal management system for electric vehicles," *Energy Convers Manag*, vol. 207, Mar. 2020, doi: 10.1016/j.enconman.2020.112569.

[49] Y. Deng *et al.*, "Effects of different coolants and cooling strategies on the cooling performance of the power lithium ion battery system: A review," Sep. 01, 2018, *Elsevier Ltd*. doi: 10.1016/j.applthermaleng.2018.06.043.

[50] J. W. Han, K. S. Garud, E. H. Kang, and M. Y. Lee, "Numerical Study on Heat Transfer Characteristics of Dielectric Fluid Immersion Cooling with Fin Structures for Lithium-Ion Batteries," *Symmetry (Basel)*, vol. 15, no. 1, Jan. 2023, doi: 10.3390/sym15010092.

[51] R. Jin, W. Chen, and A. Sudjianto, "An efficient algorithm for constructing optimal design of computer experiemnts," *J Stat Plan Inference*, vol. 134, pp. 268–287, Jul. 2004, doi: https://doi.org/10.1016/j.jspi.2004.02.014.

[52] A. J. Smola, B. Sch¨olkopf, and S. Sch¨olkopf, "A tutorial on support vector regression *," Kluwer Academic Publishers, 2004.

[53] P. Anand, R. Rastogi, and S. Chandra, "A class of new Support Vector Regression models," *Applied Soft Computing Journal*, vol. 94, Sep. 2020, doi: 10.1016/j.asoc.2020.106446.

[54] M. D. Buhmann, "Radial basis functions," *Acta Numerica*, vol. 9, pp. 1–38, Jan. 2000, doi: 10.1017/S0962492900000015.

[55] Z. Sui, H. Lin, Q. Sun, K. Dong, and W. Wu, "Multi-objective optimization of efficient liquid cooling-based battery thermal management system using hybrid manifold channels," *Appl Energy*, vol. 371, Oct. 2024, doi: 10.1016/j.apenergy.2024.123766.

[56] D. Dutta, H. Zhang, and B. Bhatia, "Multi-objective optimization of pyroelectric thermal-electrical cycles," *AIP Adv*, vol. 12, no. 7, Jul. 2022, doi: 10.1063/5.0082250.

[57] L. Sheng *et al.*, "Numerical investigation on a lithium ion battery thermal management utilizing a serpentine-channel liquid cooling plate exchanger," *Int J Heat Mass Transf*, vol. 141, pp. 658–668, Oct. 2019, doi: 10.1016/j.ijheatmasstransfer.2019.07.033.

[58] Y. Li, Z. Zhou, and W. T. Wu, "Three-dimensional thermal modeling of Li-ion battery cell and 50 V Li-ion battery pack cooled by mini-channel cold plate," *Appl Therm Eng*, vol. 147, pp. 829–840, Jan. 2019, doi: 10.1016/j.applthermaleng.2018.11.009.

[59] A. Adeniran, J. Bak, B. Bhatia, and S. Park, "Optimizing single-phase immersion cooling system for lithium-ion battery modules in electric vehicles: A multi-objective design approach," *International Journal of Thermal Sciences*, vol. 210, Apr. 2025, doi: 10.1016/j.ijthermalsci.2024.109636.

[60] L. Sheng, C. Zhang, J. Xu, Q. Zhou, and X. Zhang, "Quantitative measurement of thermal performance of a cylindrical lithium-ion battery," *Measurement (Lond)*, vol. 239, Jan. 2025, doi: 10.1016/j.measurement.2024.115458.

[61] S. Panchal, I. Dincer, M. Agelin-Chaab, R. Fraser, and M. Fowler, "Experimental and simulated temperature variations in a LiFePO4-20 Ah battery during discharge process," *Appl Energy*, vol. 180, pp. 504–515, Oct. 2016, doi: 10.1016/j.apenergy.2016.08.008.

Appendix A.

Table 6. Thirty-five DOE points with CFD results for three objectives.

Design Point #	Design parameter		Response		
	h_b (mm)	W_c (mm)	T_{max} (°C)	T_{diff} (°C)	ΔP (Pa)
1	8.264	14.01	30.09	3.98	76.565
2	9.343	12.8	30.51	4.245	53.383
3	3.391	8.271	30.05	4.125	447.12
4	3.487	10.84	29.538	2.925	538.89
5	4.622	7.75	30.466	4.368	178.23
6	4.039	14.46	31.57	5.87	517.292
7	7.445	9.894	30.675	4.362	67.884
8	5.396	11.61	29.942	3.974	178.424
9	4.134	12.31	29.647	3.868	399.499
10	8.864	7.004	31.682	4.91	42.514
11	4.875	5.695	31.149	4.73	125.523
12	8.026	7.997	31.24	4.673	51.25
13	4.543	10.47	29.946	4.01	253.21
14	7.133	14.1	29.913	3.875	108.459
15	9.559	9.124	31.293	4.745	39.674
16	6.524	10.74	30.284	4.132	100.167
17	5.55	9.359	30.331	4.189	132.066
18	8.543	9.531	31.037	4.572	49.611
19	9.083	11.27	30.762	4.4	49.837
20	7.75	12.07	30.324	4.16	74.716
21	5.13	13.68	29.663	3.768	247.845
22	5.981	14.76	29.666	3.752	179.786
23	7.544	5.307	31.935	5.015	56.775
24	9.862	7.317	31.774	4.955	36.898
25	6.295	12.59	29.948	3.915	130.059
26	3.085	13.31	29.326	2.92	945.47
27	5.813	6.519	31.128	4.646	90.435
28	6.628	8.667	30.77	4.469	79.874
29	3.691	6.247	30.654	4.495	265.659
30	7.057	6.926	31.3	4.699	62.204
31	9.232	5.516	32.37	5.328	44.642
32	3	5	30.886	4.738	377.697
33	10	5	32.822	5.764	45.431
34	3	15	29.205	2.74	1177.3783
35	10	15	30.18	4	56.69